Check for updates

Assessing half-Heusler alloys PtNbZ (Z=Al, Ga, In) *via* DFT: acceptability for thermoelectric applications

Danish Abdullah, [ID] *[a] Sakshi Gautam, [ID] [b] Ab Quyoom Seh, [ID] [b] Shabir Ahmad Mir [ID] [b] and Dinesh C. Gupta [ID] [b]

The current study relies on the investigation of PtNbZ (Z = Al, Ga, In) half-Heusler alloys using two distinct methods: the generalized gradient approximation (GGA) and a modified version of the Beck–Johnson potential. The structural parameters and ground state are obtained by optimizing the alloys in various structural phases using the GGA technique, and the findings show that the alloys crystallize in the Y_1 phase with non-magnetic spin ordering. With zero net magnetic moments, these alloys perfectly follow the Slater–Pauling rule $M_T = Z_T - 18$. The elastic parameters determine the structural stability and anisotropic character of the medium. For varied direction-dependent sound velocities, the alloys investigated are ductile, with the Debye temperatures being 423.53, 451.66 K, and 392.97 K, respectively. The alloys possess high figure of merit (ZT) values of 0.59, 0.76 and 0.78, respectively, suggesting their applications in thermoelectric power generation.

1. Introduction

Devices based on conventional semiconductor electronics utilize the charge transport properties of an electron and completely ignore its spin degree of freedom. These devices experience severe heating effects, slow data and information processing speeds, limited data storage capacity, volatility of memory elements and high-power consumption, and have limited functionalities. These problems primarily arise from transistor heating and charge leakage of capacitors, which consequently affect the performance of appliances. There is a pressing need to create a new paradigm of devices that make use of electron[1-3] spin, and the study of such devices is referred to as spintronics. The first experimental realization of a spin-dependent device occurred in 1988 when two groups led by Albert Fert[4] and Peter Grünberg[5] independently studied magnetic multilayer systems separated by a non-magnetic layer and concluded that the resistance was dependent on the spin of the electrons, called giant magnetoresistance (GMR).[6-10]

Up to now, various spintronic devices have been fabricated, which include GMR, Spin Valve systems and tunnelling magnetoresistance devices. These devices (GMR, Spin valve, and TMR) consist of ferromagnetic materials separated by a non-magnetic (NM) metal, an NM semiconductor and an ultra-thin insulator, respectively. The layer that separates the FM materials is called the spacer layer. The efficiency of these devices depends on the

spin polarization of the materials and the spacer layer. The most compatible materials for spintronics are half-metals or spin-gapless semiconductors. However, it has been found that the spin polarization is also dependent on the spacer layer. The conductive spacer layers, due to their magnetic anisotropy and stray fields, affect the spin polarization. As semiconductors do not conduct at lower temperatures, it is very hard to customise the properties of spin-dependent devices. Hence, our main focus is on analysing the new semi-metallic half-Heusler alloys PtNbZ (Z = Al, Ga, In), which will act as spacer layers in GMR and spin valves. In addition to this, it has been found that the non-magnetic materials also exhibit spin polarization, but the materials must be non-centrosymmetric (without inversion symmetry). The spin polarization in non-magnets arises due to the spin Hall, Bychkov–Rashba and Dresselhaus effects.

Apart from spintronics applications, the material must have an efficient thermoelectric figure of merit (ZT). This explains the material's efficacy in converting waste heat into usable electrical energy by leveraging the Seebeck effect. Concerning spin-dependent applications and thermoelectric efficiency, a wide range of materials, including Pnictides, Clathrates, Chalcogenides, Skuttrides, Perovskites, and Heusler alloys, have been studied theoretically and experimentally. Heusler alloys have a high Curie temperature, 100% spin polarisation, and efficient thermoelectric properties.[11-17] However, there are only a few non-magnetic semiconducting Heusler alloys. We will study the novel non-magnetic semi-metallic family PtNbZ (Z = Al, Ga, In) in light of the above-mentioned features and the non-centrosymmetric symmetry of Heusler alloys. Because no theoretical or experimental data on

[a]Department of ECE, School of Engineering, SR University, Warangal, 506371, Telangana, India. E-mail: danish.abdullah@sru.edu.in

[b]Condensed Matter Theory Group, School of Studies in Physics, Jiwaji University Gwalior, 474011, India. E-mail: danishmir1650@gmail.com

these alloys are available, our findings will serve as guidelines for future theoretical and experimental analysis.

2. Computational methodology

DFT (density functional theory) modulation is a powerful tool to emphasize the nature of any material. The essence of these techniques is first-principle simulations. The preset DFT analysis of PtNbZ (Z= Al, Ga, In) alloys was carried out using the Wien2k package, which is based on the full-potential linearized augmented plane wave method (FP-LAPW). The geometrical optimization was performed using the generalized gradient approximation (GGA).[18] The unit cell is separated into non-overlapping spheres having a spherical wave function and an interstitial region having plane wave character, and the $R_{MT}K_{max}$ was set to 7, where K_{max} is the largest plane wave cutoff and R_{MT} is the smallest muffin tin radius. For Brillouin zone integration, we used a dense k-mesh of 3000 points and the cutoff energy, which separates valence and core electrons, is set to -7 Ry. The electronic structure of these alloys was scrutinized by adopting the Perdew–Burke–Ernzerhof version of the generalized gradient approximation (GGA–PBE) as the exchange–correlation term.[18] As the GGA produces erroneous results due to self-interaction, the continuity of density derivatives is not suitable for large systems, and hence further amendments are required. In 2006, Becke and Johnson[19] introduced a new potential term for exchange and correlation, but it could not provide sufficiently accurate results. It was subsequently modified by Fabien Tran and Peter Blaha,[20] though for some systems this also did not yield precise results. Therefore, David Koller, Fabien Tran, and Peter Blaha further refined it through reparameterization and the use of different data sets.[21]

The group concluded that it can be employed to any system or material with accuracy of results much better than various expensive computational methods, including the GW method. Concerning these discrepancies and keeping in view the accuracy of mBJ, we will explore our results through the mBJ method.[21] Self-consistency is obtained by setting the charge and energy convergence to 0.0001 Ry and 0.0001e. The mechanical stability of the alloys was determined using the Elastic Code of Murtaza Jamal integrated into Wien2k.[22] The transport properties of the present alloys were determined using the BoltzTraP2 code embedded in Wien2k.[23] The BoltzTaP2 Code utilizes the Boltzmann Transport equation (BTE), which is a complicated non-linear integral-differential equation and very complicated. The solution of this equation is obtained by using some assumptions. One such assumption is relaxation time approximation (RTA) with $\tau = 0.5 \times 10^{-14}$ s and is based on the fact that thermoelectric parameters do not vary readily with energy on the K_BT scale.[23] The electrical conductivity (σ) and electronic thermal conductivity (κ_e) and the Seebeck (S) coefficients can be determined through the relations:

$$k_e = K_B{}^2 T \int \left(\frac{-\partial f_0}{\partial E}\right)\left(\frac{\varepsilon - \mu}{K_B T}\right)^2 \varXi(\varepsilon)\mathrm{d}\varepsilon(\varepsilon) = \sum_K \delta(\varepsilon - \varepsilon_K)\nu_K{}^\alpha \nu_K{}^\beta \tau_K;$$

$$S = \frac{eK_B}{\sigma}\int\left(\frac{-\partial f_0}{\partial E}\right)\frac{\varepsilon - \mu}{K_B T}\varXi(\varepsilon)\mathrm{d}\varepsilon; \quad \sigma = \int\left(\frac{-\partial f_0}{\partial E}\right)\varXi(\varepsilon)\mathrm{d}\varepsilon$$

where $\nu_K{}^\alpha$ depicts the α component of the group velocity with wave vector k.

To determine the transport coefficients, a large k-point mesh of 150 000 k points was used to obtain more precise results.

3. Results and discussions

3.1 Structural properties

The general stoichiometric composition of full Heusler alloys is X_2YZ, where X and Y are transition metal atoms and Z is an s or p block element. These alloys crystallize in the L_{21} structure with the $Fm\bar{3}m$ space group and prototype structure Cu_2MnAl. The L_{21} unit cell consists of four interpenetrating FCC lattices and is an ordered structure. The site occupancy of the atoms at different

Table 1 Different phases of half-Heusler alloys with the Wyckoff positions

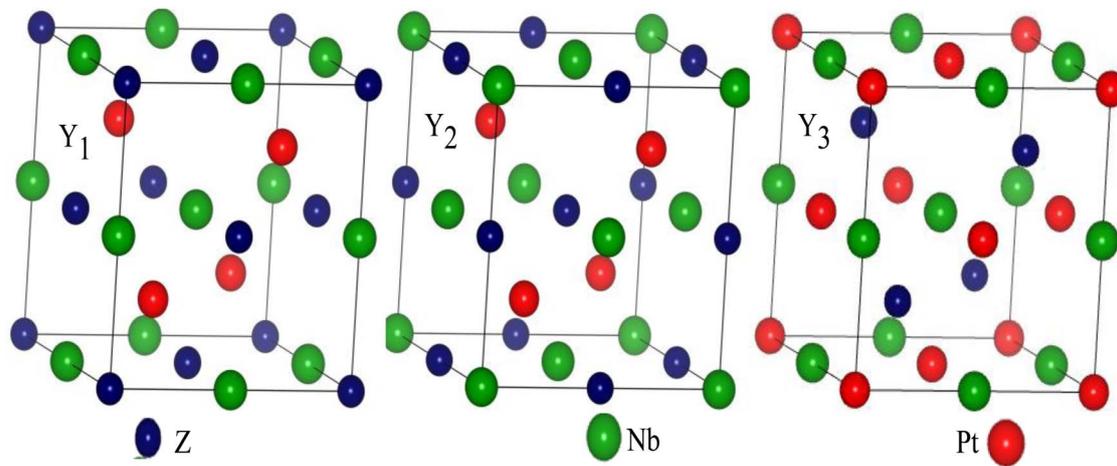| Type	4a (0,0,0)	4b (1/2,1/2,1/2)	4d (3/4,3/4,3/4)
Y_1	Z	Nb	Pt
Y_2	Nb	Z	Pt
Y_3	Pt	Nb	Z

Fig. 1 (Y1, Y2, Y3) Various structural variants of half-Heusler alloys.

Wyckoff positions depends on several factors: (a) the valence electron count of atoms X, Y and Z and (b) the electronegativity and chemical environment of the atoms. If one of the X atoms is completely removed, then the alloy obtained is called a half-Heusler alloy and the structural symmetry of this alloy is reduced to a non-centrosymmetric ($F\bar{4}3m$) group, which means that inversion symmetry is wiped out.[24] Due to this symmetry breakdown and depending upon site occupancy, three different structural variants are possible, referred to as Y_1, Y_2 and Y_3. The site occupancy and Wyckoff positions of the various structural phases are presented in Table 1, and the structures are shown in Fig. 1 (Y_1, Y_2, Y_3). The Y_1-type is the most frequently obtained structure if the number of valence electrons of X is large, as compared to other atoms. The atoms in the unit cell are oriented in tetrahedral and octahedral geometries. The Wyckoff positions 4a and 4c form a ZnS-type lattice (tetrahedron) having covalent

bonding interactions. The atoms at the 4a and 4b positions are such that they form an NaCl-type sublattice (octahedron) with strong ionic bonding, and alloys that have both ionic and covalent bonding interactions are called polar covalent. We have optimized the total energy *vs.* unit cell volume in all three phases and the most stable state among the three is in the non magnetic phase. The optimization plots are profiled in Fig. 2a–c which makes it clear that the alloys crystallize in the Y_1-type structure. The various equilibrium lattice parameters like a, bulk modulus (B), and pressure derivative of the bulk modulus (B_0'), along with the total, are presented in Table 2.

3.2 Elastic properties

Elastic metrics assess how a material behaves under numerous external constraints (loads, forces, and pressures). These attributes outline the material's resistance to external stresses, as
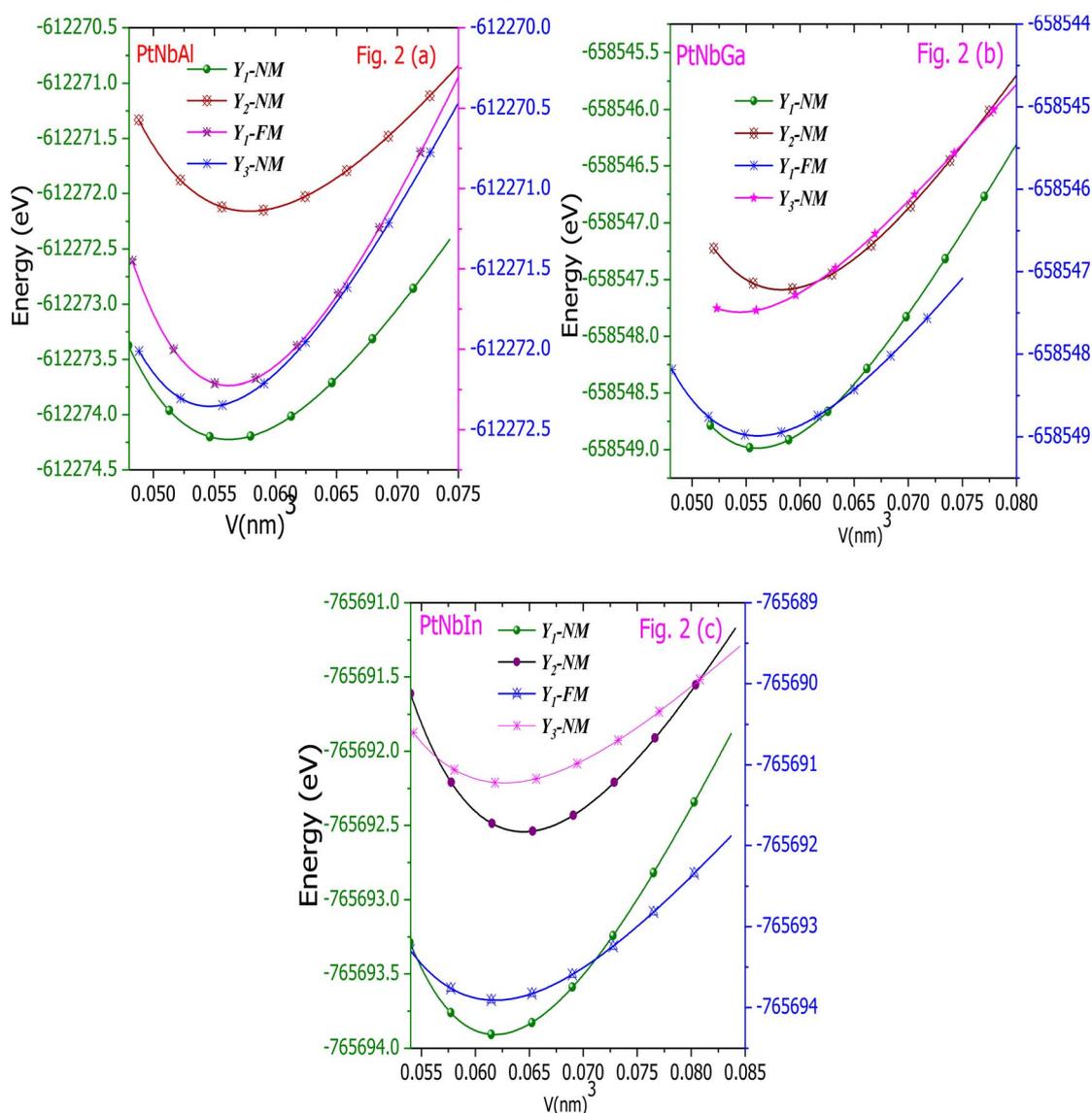

Fig. 2 (a–c) Structural optimization of PtNbZ (Z = Al, Ga, In) alloys of different structural types.

Table 2 Optimization of parameters such as volume (nm),[3] bulk modulus (B in GPa) and its pressure derivative (B_0'), ground state energy (eV) and relaxed lattice constant (nm) of the PtNbZ (Z = Al, Ga, In) alloys

	Phase	a	V	B	B_0'	E_0
PtNbAl	Y$_1$	0.6080	0.056174	168.24	4.52	−612 274.22
	Y1-FM	0.6061	0.055584	163.27	4.48	−612 274.13
	Y$_2$	0.6142	0.05785	136.01	4.43	−612 272.16
	Y$_3$	0.6022	0.054592	144.21	4.49	−612 272.35
PtNbGa	Y$_1$	0.60745	0.055997	165.71	4.56	−658 549.22
	Y1-FM	0.6059	0.054634	158.41	4.47	−658 549.57
	Y$_2$	0.61552	0.058282	138.31	4.63	−658 548.59
	Y$_3$	0.60165	0.054362	157.51	4.74	−658 547.49
PtNbIn	Y$_1$	0.62775	0.061829	151.9001	4.71	−765 694.90
	Y1-FM	0.62542	0.061195	148.567	4.05	−765 694.82
	Y$_2$	0.6366	0.064474	124.0861	4.77	−765 693.54
	Y$_3$	0.63068	0.062698	130.3344	4.92	−765 691.22

Table 4 Calculated average sound velocity (m s^{-1}), Debye temperature (K), and Poisson's ratio (σ)

Parameter	v_t	v_l	v_m	θ_D	σ
PtNbAl	2951	5444	3819	423	0.26
PtNbGa	2921	5243	3826	451	0.29
PtNbIn	2506	4738	3293	392	0.30

well as the limits to which it is mechanically operating. Mechanical robustness represents one of the prerequisites that materials must accomplish prior to being utilized in engineering buildings and smart material technological advances. Elastic constants (E_C) act as mechanism as they are associated with multiple thermodynamic traits, which consequently pertain to the material's physical properties. The mechanical stability is estimated by acquiring the elastic stiffness coefficients (C_{ij}s). These C_{ij}s are heavily reliant on the symmetry of the crystal structure. Cubic crystals have three C_{ij}s, that is C_{11}, C_{12} and C_{44}, where C_{11} confirms the material's stiffness and symbolizes longitudinal compression or elongation, or transition along the uniaxial axis. The transverse expansion, or distortion, is marked by C_{12} and correlates with Poisson's ratio. The shear elastic dimension, which is contingent on the shear modulus, is assigned by C_{44}. As more accurate methods are needed to assess the overall energy or stress after strain, one must exercise extreme caution when figuring out these quantities using DFT methods. Table 3 displays the E_C values for the alloys that are being examined, from which it is obvious that everything operates positively and adheres to the Born–Huang criteria:[25] $C_{11} - C_{44} > 0$; $C_{11} + 2C_{12} > 0$; $C_{11} - C_{12} > 0$. Other elastic properties can be clarified among these parameters.

The Voigt–Reuss–Hill averaging algorithm [26,27] was implemented to figure out the elastic moduli, namely the shear and bulk moduli. For cubic crystals, the Voigt restrictions are $B_V = \frac{(C_{11} + 2C_{12})}{3}$; $G_V = \frac{(C_{11} - C_{12} + 3C_{44})}{5}$. The Reuss formulism is supplied by $B_V = BR$; $G_R = \frac{5(C_{11} - C_{12})C_{44}}{4C_{44} + 3(C_{11} - C_{12})}$,

whereas Hill's approximation is derived by averaging both the Voigt and Reuss approaches, $\frac{B_V + B_R}{2}$; $G = \frac{G_V + G_R}{2}$;

The shear and bulk moduli measure the alloys' stiffness and compressibility. The results retrieved for both parameters are listed in Table 3. These numbers suggest that the alloy is resilient to shape and volume deformations, while also being compressible, as the B values are appropriate. It is also visible that the values of B generated by the Brich–Murnaghan equation and the Cubic Elastic code are almost identical, demonstrating the accuracy of the results. The relations[28] are applicable to derive additional elastic parameters, including Poisson's ratio (ν), anisotropic factor (A), and Young's modulus (E).

$$E = \frac{9BG}{3B + G} \quad \sigma = \frac{3B - 2G}{2(3B + G)}$$

Young's modulus (Y), which reflects a metric of stress to strain and is expressed as $Y = \frac{9BG}{3B + G}$, implies how rigid the materials are. While small values of Y reflect ductile character, large values prove the brittle nature of materials. Pugh's ratio and Cauchy pressure may be employed to confirm this. One can figure out the malleability, ductility, or brittleness by computing Cauchy's pressure ($C_P = C_{12} - C_{44}$) and the Pugs ratio (B/G, limiting value 1.75). Table 3 summarizes the acquired data. It is clear that both alloys have B/G ratios larger than 1.75 and that C_P is positive, both of which demonstrate the alloys' ductility.

Debye temperature (θ_D), another important parameter, can be calculated using the relation $\theta_D = \frac{h}{k}\left[\frac{3n}{4\pi}\frac{N_A\rho}{M}\right]^{\frac{1}{3}}v_m$. The values of θ_D for the alloys under study have been obtained from the average sound velocities given by the equation $v_m = \left[\frac{1}{3}\left(\frac{2}{v_t^3} + \frac{1}{v_t^3}\right)\right]^{\frac{-1}{3}}$, where v_l and v_t represent longitudinal and transverse sound velocities given by $v_l = \sqrt{\frac{3B + 4G}{3\rho}}$ and $v_t = \sqrt{\frac{G}{\rho}}$, respectively.

Table 3 Calculated values of elastic constants C_{11}, C_{12} and C_{44} in GPa, Young's modulus Y (GPa), bulk modulus B (GPa), shear modulus G (GPa), and Zener anisotropy factor (A)

Alloy	C_{11}	C_{12}	C_{44}	B	G_R	G_V	G	B/G	Y	C_P	A
PtNbGa	224.35	142.62	123.54	169.86	90.47	68.28	79.37	2.13	206.04	19.07	3.02
PtNbAl	253.07	125.80	118.27	168.22	96.42	88.03	92.22	1.82	233.93	7.525	1.85
PtNbIn	205.82	125.26	96.37	152.11	73.93	61.89	67.91	2.23	177.35	28.89	2.39

Table 5 PtNbZ (Z = Al, Ga, In): direction-dependent longitudinal and transverse sound velocities (m s^{-1})

Propagation direction	Mode of vibration	C_{eff}	Al	Ga	In
[100]	v_l	C_{11}	4911.62	4888.49	4363.49
	$v_{t1} = v_{t2}$	C_{44}	3644.79	1760	3341.95
[110]	v_l	$(C_{11} + C_{12} + 2C_{44})/2$	5745.82	5390.44	4922.37
	v_{t1}	C_{44}	2096.20	2451.33	1930.27
	v_{t2}	$(C_{11} - C_{12})/2$	3644.79	3644.79	2985.90
[111]	v_l	$(C_{11} + 2C_{12} + 4C_{44})/3$	5998.16	5547.68	5095.06
	$v_{t1} = v_{t2}$	$(C_{11} - C_{12} + C_{44})/3$	2712.48	2780.09	2335.77

The calculated values of θ_D are presented in Table 4. It acts as a barrier that distinguishes the high and low-temperature regimes of alloys. The values of θ_D for the alloys under study have been obtained from average sound velocities given by the above equations.

As described above, both materials exhibit anisotropy, so the motion of sound velocities will be direction-dependent. For anisotropic crystals, there is one longitudinal velocity (in which the direction of the wave and motion of the particles are along the same axis) and two transverse velocities (in which wave
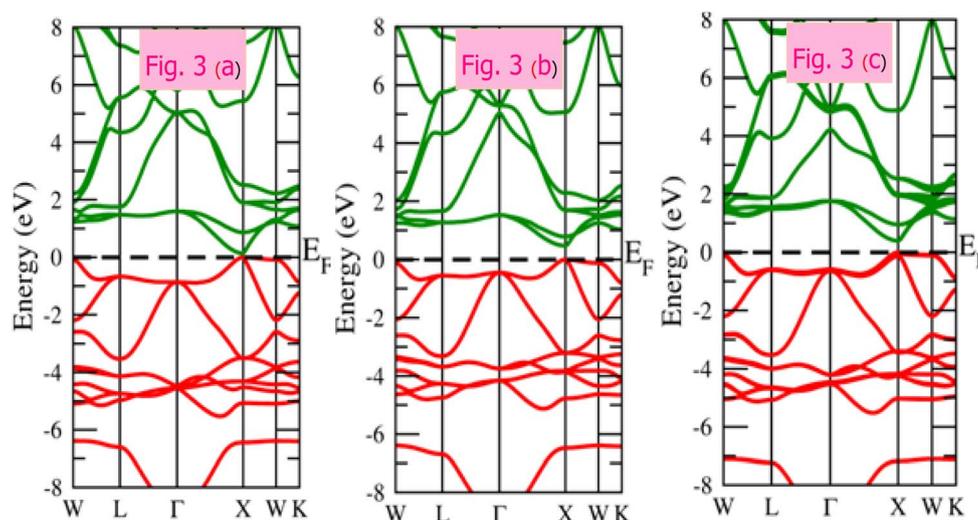
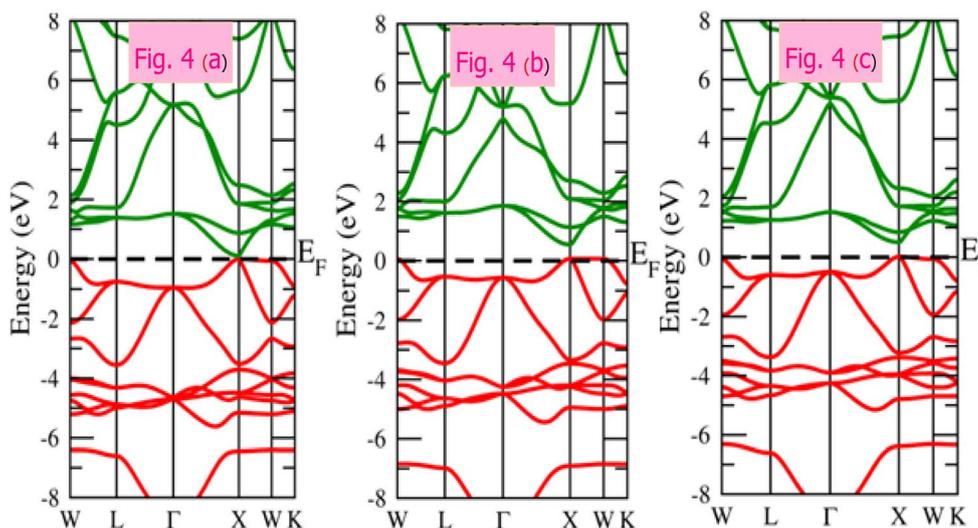**Fig. 3** (a–c) Band structure of PtNbZ (Z = Al, Ga, In) under GGA approximation.

Fig. 4 (a–c) Band structure of the PtNbZ (Z = Al, Ga, In) alloys under the mBJ method.

Table 6 The calculated band gap (in eV) of the PtNbZ (Z = Al, Ga, In) alloys under the GGA and mBJ schemes

Alloy	PtNbAl	PtNbGa	PtNbIn
GGA	0.14	0.39	0.46
mBJ	0.10	0.54	0.51

propagation is perpendicular to the vibration of particles). The magnitude of these velocities is calculated using a mathematical relation. Moreover, we evaluated the average values $v = \sqrt{\dfrac{C_{\text{eff}}}{\rho}}$. of longitudinal, transverse, and mean Debye velocity using the relations above. The calculated values are reported in Table 5. The purpose of calculating these velocities is to determine the extent of anisotropy along with different directions of the materials.

3.3 Band structure

The electronic nature of any material can be understood by plotting the band structure along the symmetry points of the Brillouin zone, and the nature of the bands at the Fermi level determines its category. The obtained band structures under GGA and mBJ are presented in Fig. 3a–c and 4a–c, respectively. The plots show that the valence band exactly touches the Fermi level at the X-point of the Brillouin zone, hence depicting a semi-metallic nature. Furthermore, the maximum of the valence band (VB) and minimum of the conduction band do not lie at the same symmetry point, so we can conclude that the alloys have indirect band gaps. The magnitude of the band gap is calculated and is given in Table 6. From the table, it is evident that both GGA and mBJ show differences in the band gaps, which is endorsed by the solution of the exchange-correlation potentials.

3.4 Partial density of states (PDOS)

An insight into the band structure is provided by plotting the partial density of states (PDOS) of individual atomic energy levels. The PDOS plotted under GGA and mBJ is profiled in Fig. 5a–c and 6a–c, respectively. From these results, it is obvious that the alloys exhibit semi-metallic nature. The figures confirm the splitting of all atomic energy levels at the Fermi level, which is ascribed to the complete electron filling of electrons in the Z and d-states. The
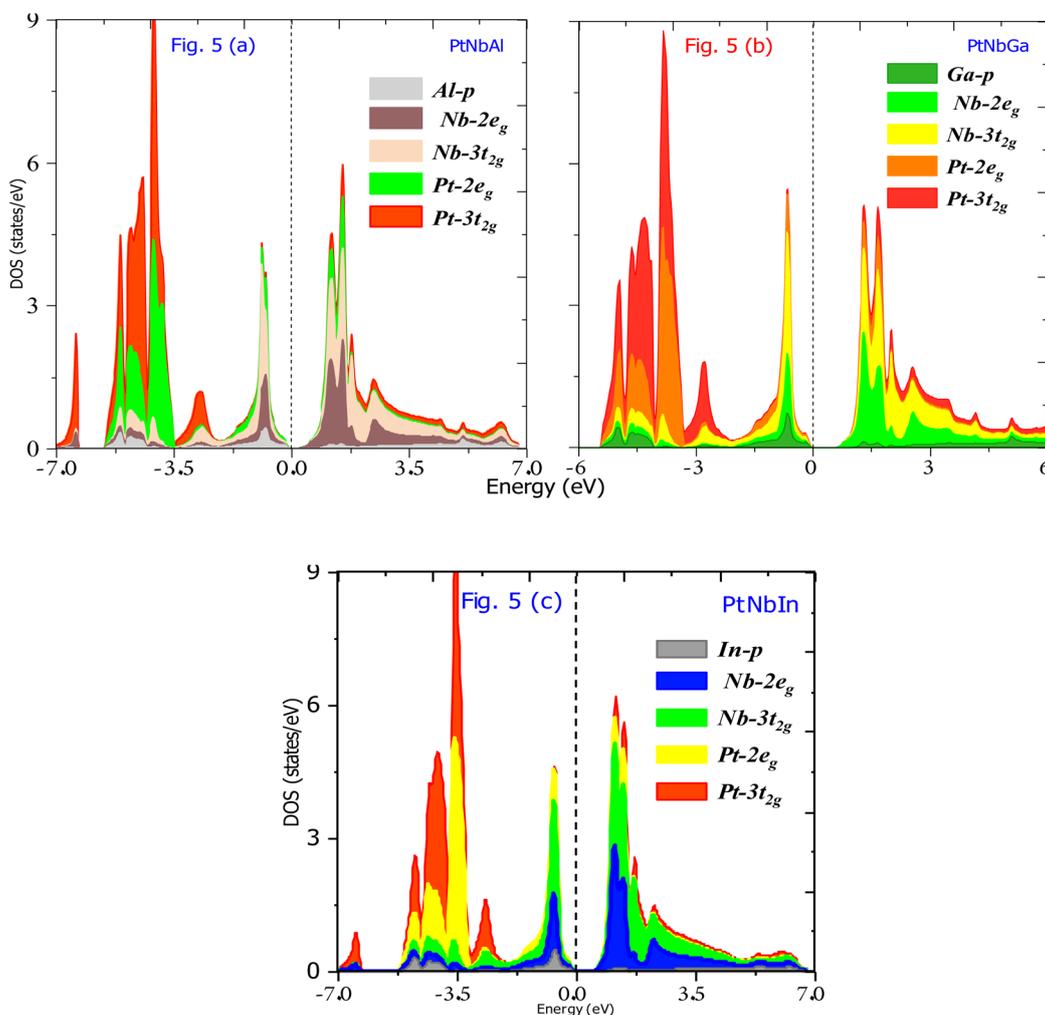

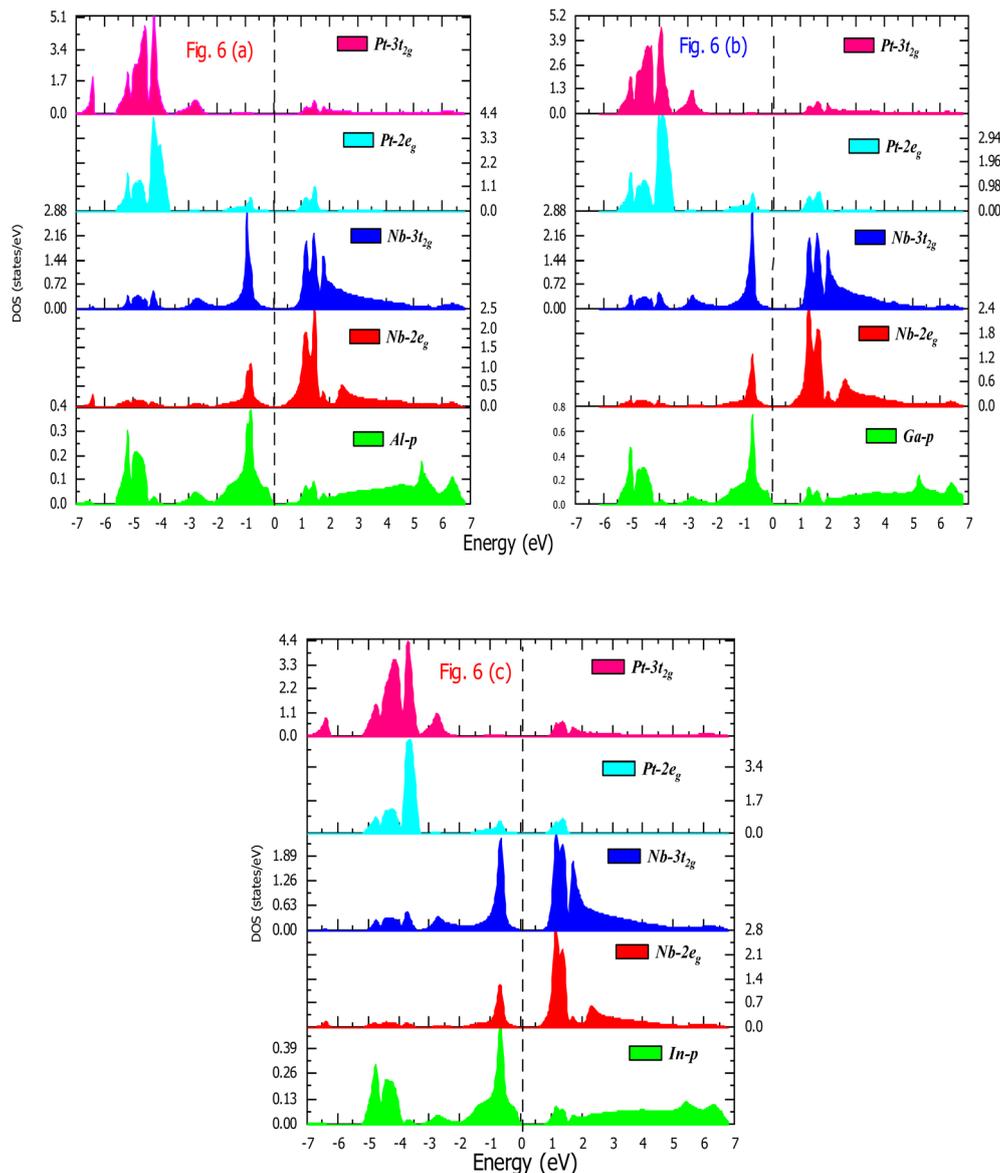**Fig. 5** (a–c) Atom-resolved PDOS of the PtNbZ (Z = Al, Ga, In) alloys under the GGA scheme.

Fig. 6 (a–c) PDOS of the PtNbZ (Z = Al, Ga, In) alloys under the mBJ scheme.

Fermi level is touched by Z-p states with a minute contribution from Nb states, whereas none of the Pt states lie at the Fermi level, which is due to its complete d-state filling, and the reason for this will be given in the origin of the gap section.

3.5 Existence of a gap

A crystal structure is fashioned by the everlasting attraction among the constituent atoms. This permanent magnetism arises due to the combination or assimilation of localized valence electron orbitals referred to as bonds. There are various mechanisms responsible for bond formation in materials: (i) complete charge transfer (ionic bonds), (ii) d–d orbital hybridization and (iii) covalent bonds. In the case of Heusler alloys, it has been found that d–d hybridization is dominant with a significant effect of the SP atom.[28] We will try to describe the

origin of the gap using a schematic representation of the orbitals by making use of PDOS. In the case of transition metal complexes, the crystal field splitting will take place mainly due to the electric field created by neighbouring constituents and Jahn–Teller distortion to minimize the energy of the transition metal complexes.[29] Due to this, there will be the formation of bonding ($3t_{2g}$, $2e_g$) and anti-bonding ($3t_{1u}$, $2e_u$) states for each atom. The filled bands will lie in the valence band and their anti-bonding states in the conduction band.

The Pt atom at the 4c site is the most electronegative (2.28 on the Pauling scale) in the 4a–4b–4c arrangement. The Z and Nb atoms both form tetrahedral geometries with Pt, since it is the most electronegative element with electronic configuration [Xe] $4f^{14}5d^96s^1$. Due to its high electronegativity and s-Rydberg destabilization, it will lodge its s-electron into the d-orbital to get filled, as shown Fig. 7 step (i).[30] This can be evidenced from
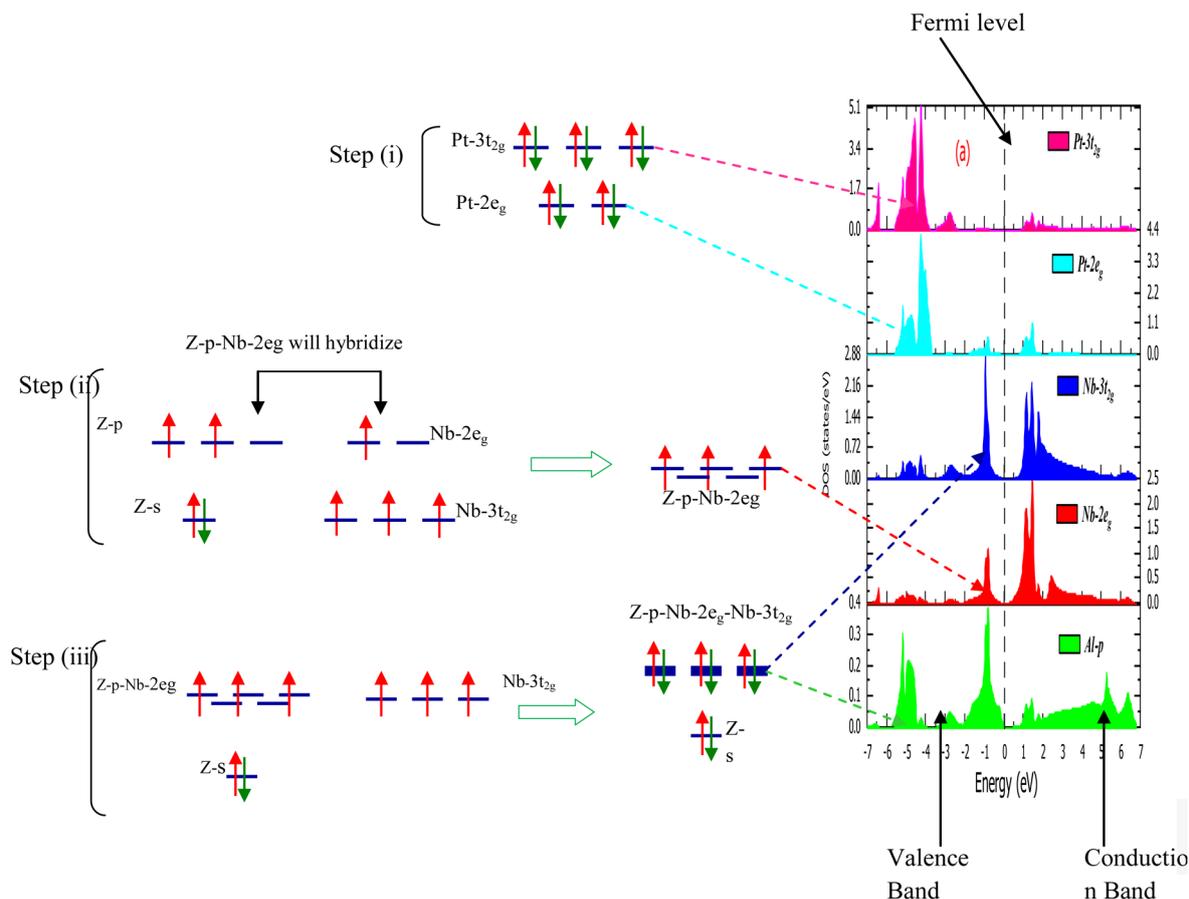
Fig. 7 (i), (ii) and (iii): (i) Electron filling of the Pt atom, (ii) hybridization of Z-p with Nb-2e$_g$, and (iii) hybridization of Z-p-Nb-2e$_g$ with Nb-3t$_{2g}$.
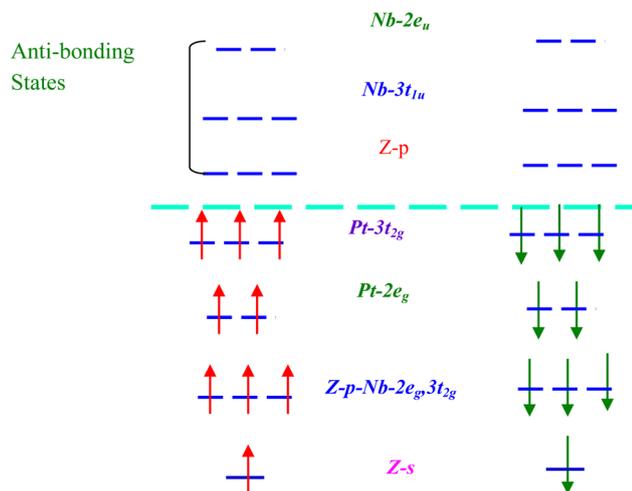

Fig. 8 The resultant hybridization of alloys, including anti-bonding states of Z and Nb, and hence confirmation of the zero magnetic moment from the Slater–Pauling rule.

Pt-3t$_{2g}$ and Pt-2e$_g$ states, which do not depict any splitting, and both states lie in the valence band and away from the Fermi level with almost zero contribution in the conduction band.

Next, we will consider the case of Z = Al, Ga, In and Nb atoms. The electronegativity of Z = Al, Ga, In and Nb is 1.61, 1.81, 1.71 and 1.60, respectively.[31] The electronic configurations are [Ne]3s^{2}3p^1, [Ar]3d^{10}4s^{2}4p^1, [Kr]4d^{10}5s^{2}5p^1 and [Kr]4d^{4}5s^1, respectively. As Z and Nb form an octahedral geometry, the 2e$_g$ state of Nb has higher energy than 3t$_{2g}$. Nb, being more electropositive among its counterparts, loses its s-electron to Z, which makes the valence electron count 4 for both atoms. Now, we will consider the hybridization of Z-p with Nb-2e$_g$, which results in a complete half-filled p-orbital, and the band has a mixed nature as depicted in step (ii) of Fig. 7. Now, the Z-p has three electrons and requires three more electrons to get filled. To get them, the resultant Z-p-Nb2eg state will further hybridize with Nb-3t$_{2g}$, which is shown in Fig. 7, step (iii), and hence the bands touch the Fermi level. Step (iii) also makes it obvious that the bonding states of the Z-p, Nb-3t$_{2g}$ and 2e$_g$ states exactly reside in the valence band with their anti-bonding states in the conduction band. To enable clear visualization of the energy states, we have omitted depicting the anti-bonds of the Z-p and Nb-d levels, which are presented in Fig. 8.

3.6 Conforming to the Slater–Pauling rule

The resultant electron filling of PtNbZ (Z = Al, Ga, In) alloys is shown in Fig. 8. As the Heusler alloys are known for their magnetic characteristics, their magnetic moment is determined
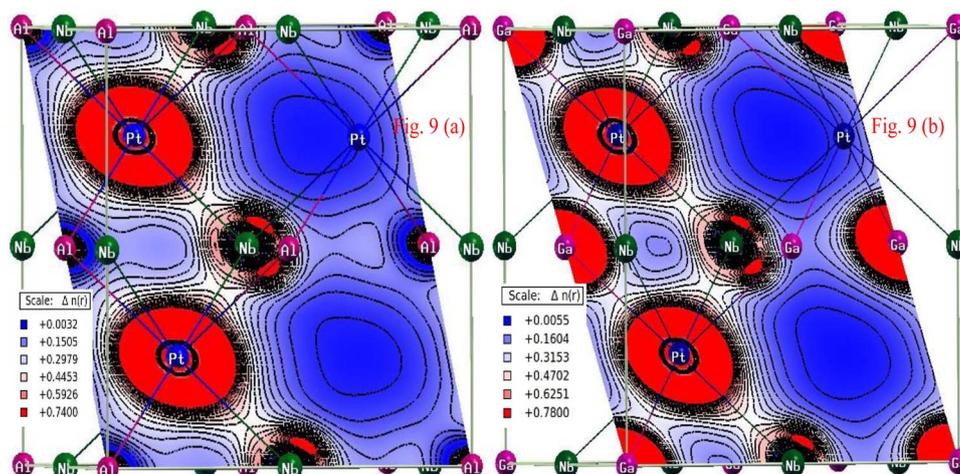
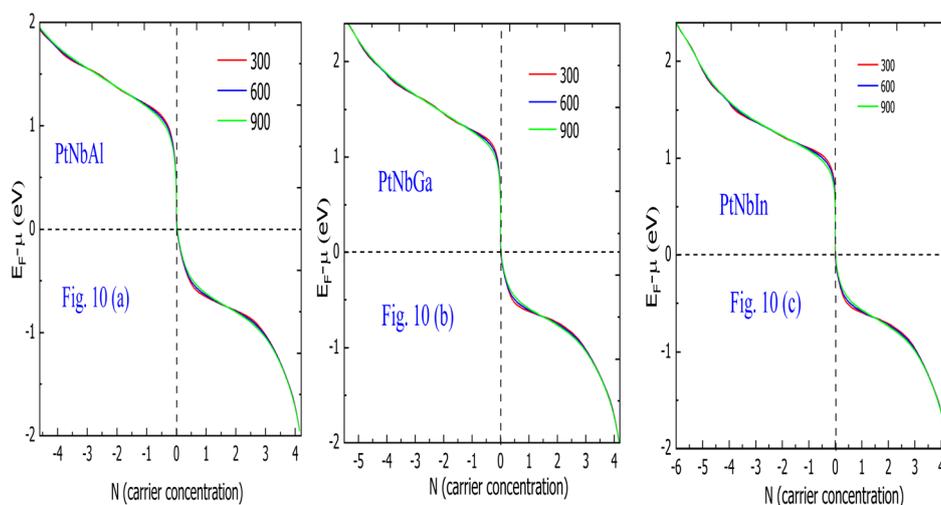**Fig. 9** (a and b) Depiction of the charge density contour plots.

Fig. 10 (a–c) Variation of carrier concentration (N) with chemical potential for PtNbZ (Z = Al, Ga, In).

using the famous Slater–Pauling rule, and the total magnetic moment is given by the number of unpaired electrons in the unit cell. The ternary Heusler alloys follow the $M_T = Z_T$-18 Slater–Pauling rule, and this rule states that the total magnetic moment of the alloys is equal to the number of unpaired electrons.[32] For the alloys under investigation, the total valence electron count (Z_T) is 18, and according to the SP rule, their magnetic moment is zero, which is evident from the total and atom-resolved magnetic moments of all alloys. Due to the complete pairing of the electron, the alloys exhibit a non-magnetic nature.

3.7 Charge density contour plots

As discussed above, the bonds may be covalent, charge transfer, or d–d hybridized, depending on the electronegativity and chemical environment of the atoms involved. The charge density contour plots are plotted and profiled in Fig. 9a and b. These atoms have electronegativity values reported above. Here, we explore the charge density of PtNbZ (Z = Al, Ga, In) alloys, of which Nb is electropositive and is bonded with Z in the vicinity of

Pt, so it will undergo chemical compression as was speculated by Pauling in 1952 and is evident from Fig. 9.[33] In transition metal complexes and intermetallic compounds, the electron transfer is governed by the electronegativity difference (from electropositive to electronegative). This results in the reduction of the gradients in potential (according to the electroneutrality principle), which can be achieved only by retransforming some electrons to the electronegative atom. In addition, the atoms that do not share electrons have exactly spherical charge density (Pt in our case), while those that share electrons for bonding have distorted or elliptical charge density surroundings (Nb and Z). The blue region depicts the vacant or empty sites in these alloys.

3.8 Thermoelectric properties

Global warming and the extinction of energy reservoirs are major challenges that the world is currently facing. The reasons for these aspects are the emission of toxicants from the combustion of fossil fuels and the exhaustion of limited energy resources. Therefore, searching for alternative ways of
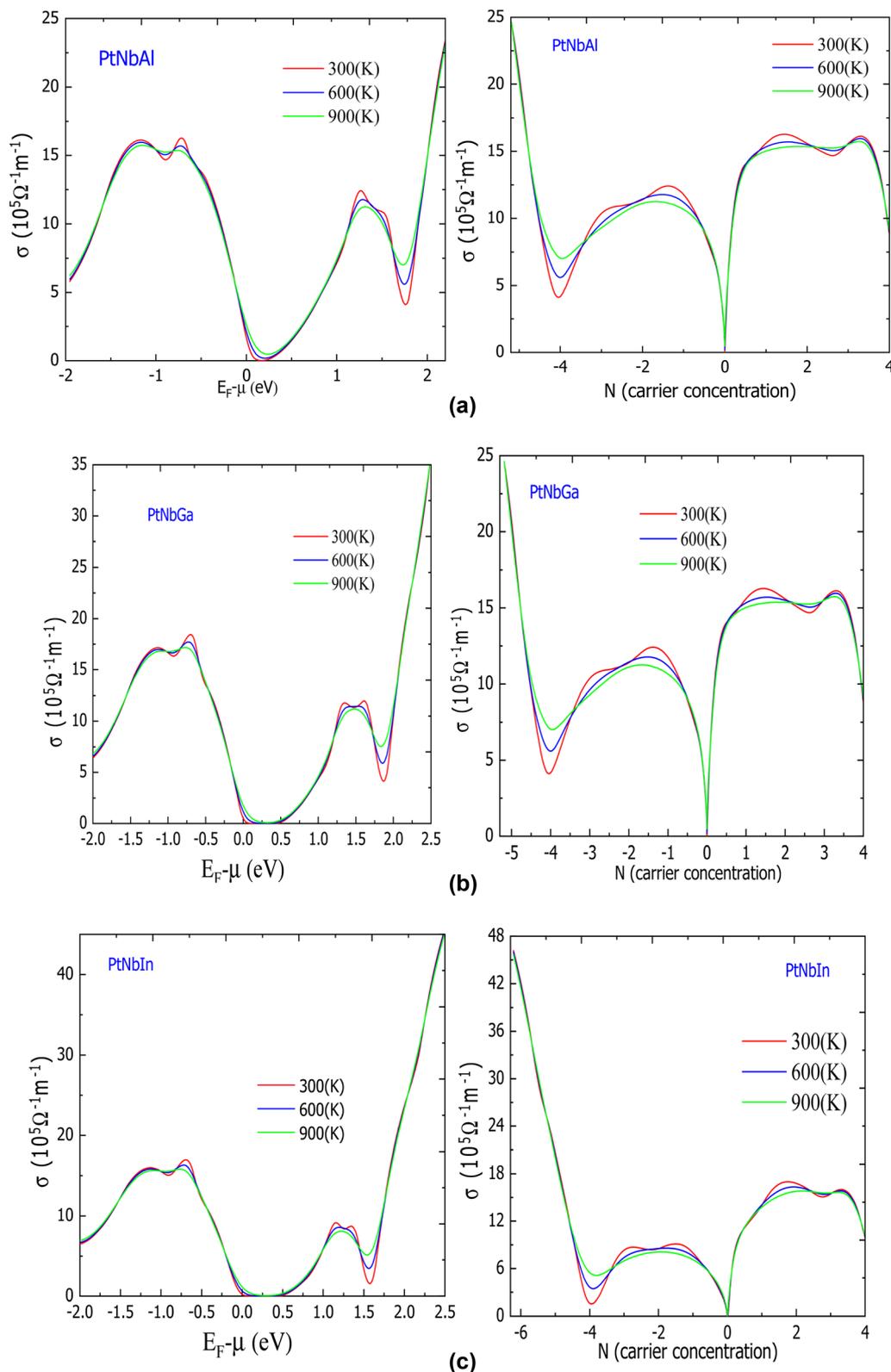
Fig. 11 (a–c) Alteration of electrical conductivity with chemical potential and carrier concentration for PtNbZ (Z = Al, Ga, In) alloys.

generating energy is necessary to save energy reservoirs and minimize the emission of toxicants and harmful gases responsible for climate change and environmental

degradation.[34,35] Possible solutions are solar energy conversion by using photo-voltaic cells and thermoelectric technology, which relies on the direct conversion of waste heat into useful
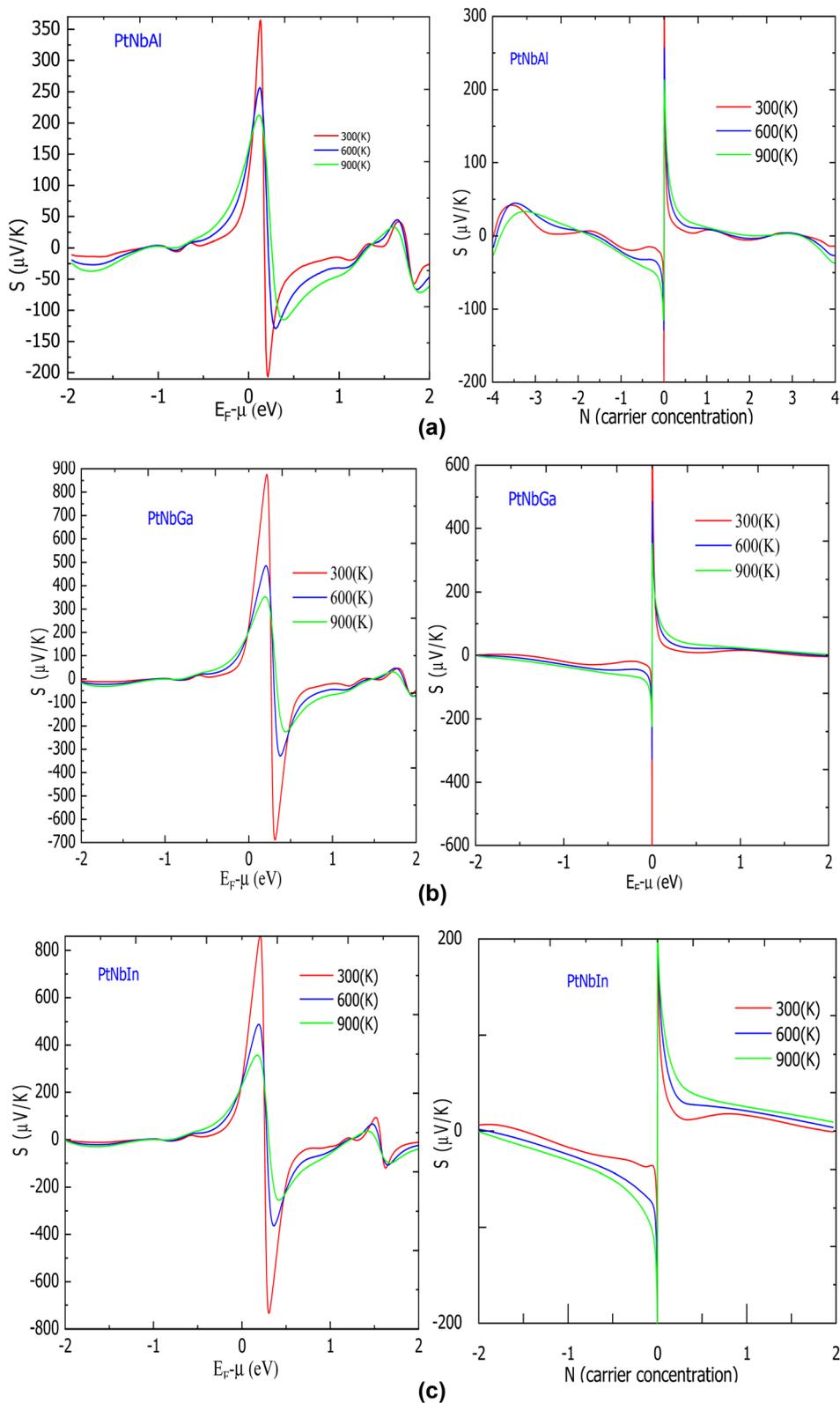
Fig. 12 (a–c) Scrutinization of the Seebeck coefficient with chemical potential and carrier concentration for PtNbZ (Z = Al, Ga, In) alloys.
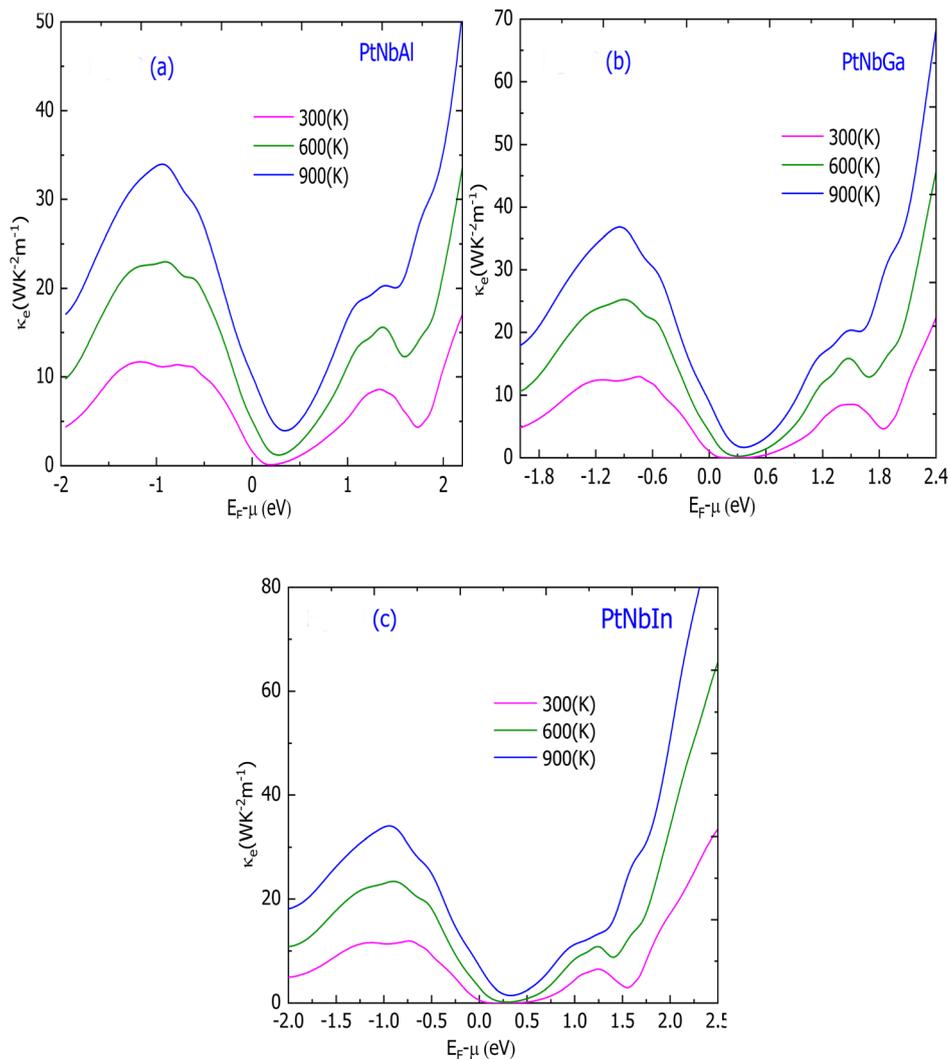
Fig. 13 (a–c) Variation of electronic thermal conductivity with chemical potential for the PtNbZ (Z = Al, Ga, In) alloys.
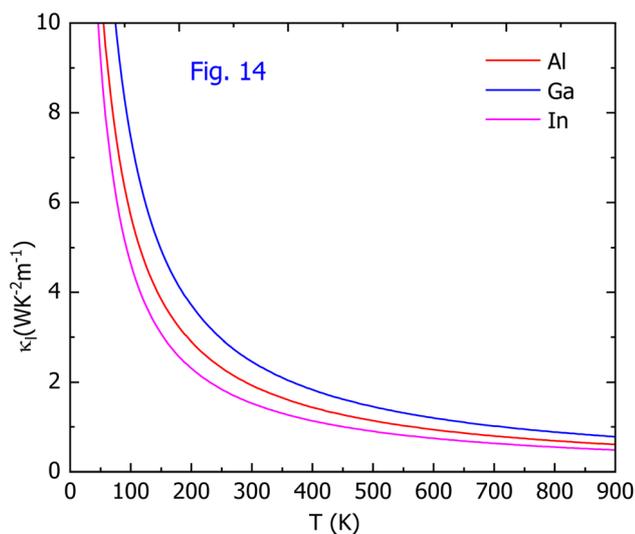

Fig. 14 Variation of lattice thermal conductivity with temperature for the PtNbZ (Z = Al, Ga, In) alloys.

electrical energy without using any moving parts or releasing fullerenes or chlorofluorocarbons. The waste heat conversion is governed by utilizing the Seebeck effect, and based on these capabilities, these materials can be exploited for waste heat scavenging and environmentally friendly refrigeration. The efficiency of thermoelectric materials is determined by a dimensionless figure of merit ZT, and the higher the value of ZT, the efficient the material will be. The various parameters on which the thermoelectric figure of merit depends were investigated and are presented below.

3.8.1 Carrier concentration (N). Carrier concentration (N) is among the prominent thermoelectric parameters that determine the efficiency of materials. Higher N means high σ and lower S, as they are mutually related. The alteration of N was plotted and is depicted in Fig. 10a–c. Concerning the plots, it is evident that N exhibits a sharp variation near zero chemical potential in the majority spin channel.[36] The metals do not exhibit any discontinuity of N at zero chemical potential, and hence, they are conducting even at zero chemical potential.

3.8.2 Electrical conductivity. The electrical conductivity (σ) of conductors/metals is due to free electrons and in semiconductors, both electrons and holes contribute to electrical conduction. In the case of semi-metals, the valence band exactly touches the Fermi level and opens a gap for the conduction band, as depicted in Fig. 4a–c, so the electrical conductivity is attributed to electrons and holes. The variation of σ at different temperatures with chemical potential and carrier concentration is profiled in Fig. 11a–c. Concerning the negative chemical potential, the σ shows a hump around −0.5 to −1.7 eV; this is due to high DOS in this region, which can be confirmed from the PDOS plots [Fig. 6a–c], and the DOS is mainly due to Z and Nb atoms. The values of σ around zero chemical potential and carrier concentration vanish, which is also evident from the plots. The reason for this is due to the absence of bands in this region. Moving towards positive values, the conductivity rises swiftly, which is supported by the increase in DOS and carrier concentration.

3.8.3 Seebeck coefficient. The Seebeck effect is a fundamental phenomenon connecting thermodynamics to electrical energy. This effect describes the voltage generation due to the temperature gradient at the ends of conductive materials. For metals and semiconductors with parabolic energy band dispersion curves, the theoretical prediction of the Seebeck coefficient can be gauged by the relation given as

$$S = \frac{8\pi^2 k^2}{3e\hbar^2} m^* T \left(\frac{\pi}{3n}\right)^{\frac{2}{3}}$$

This equation demonstrates the dependence of S on effective mass m^* and carrier concentration n. A positive value of S confirms holes as the majority carriers and a negative S value indicates electrons as the majority carriers. The variation of S with chemical potential and carrier concentration is shown in Fig. 12a–c. The electrical conductivity is directly proportional to the carrier concentration, *i.e.*, high σ corresponds to high n and *vice versa*. However, the dependence of S on n is inverse, meaning that S is high when n is low. Accordingly, S must follow this trend, and from Fig. 12, it is evident that S is highest at the lowest values
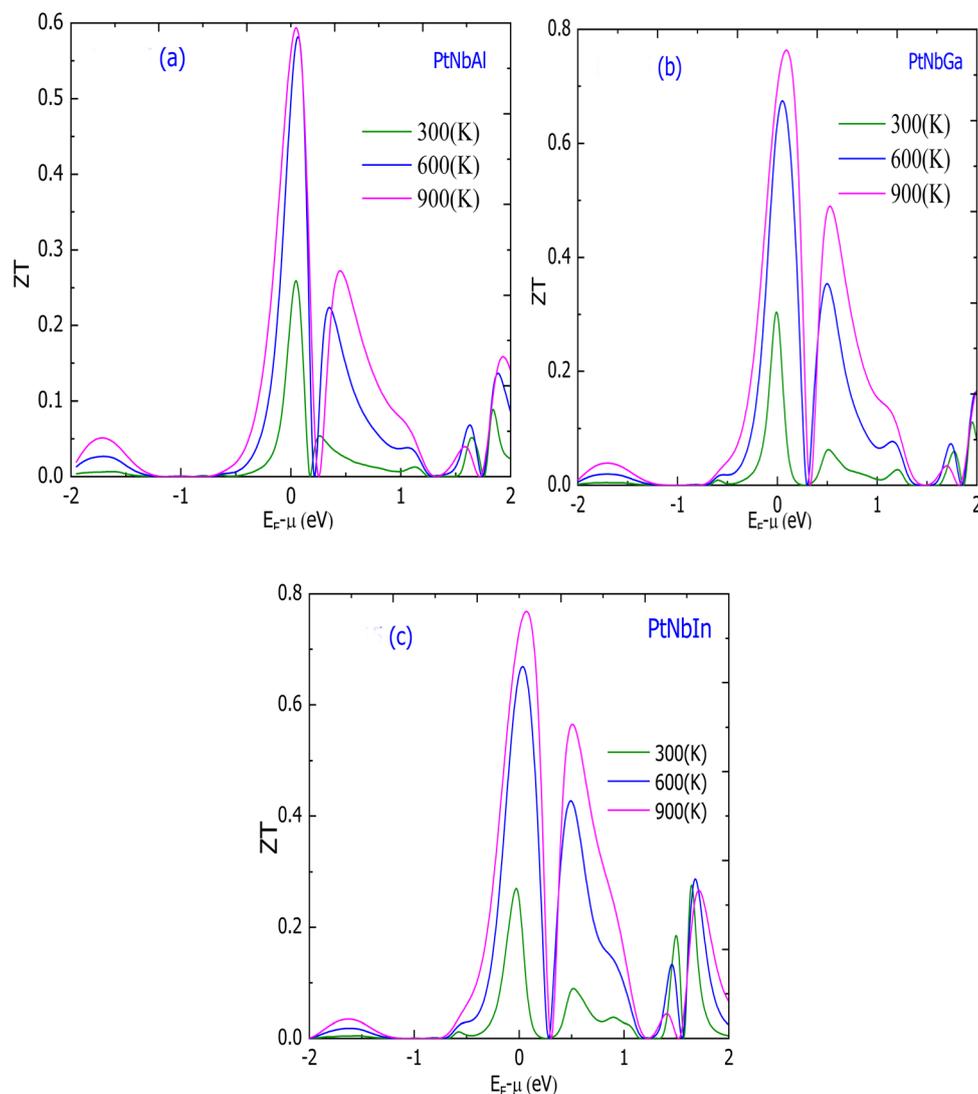

Fig. 15 (a–c) Variation of the thermoelectric figure of merit with chemical potential for the PtNbZ (Z = Al, Ga, In) alloys.

of n and σ. It is also evident that S has the highest peak at 300 K, and decreases at 600 and 900 K, respectively. This occurs because the semiconducting channel has an insignificant carrier concentration at lower temperatures. As the temperature is increases, electrons gain sufficient thermal energy and excite to the conduction band, which results in a decrease in S.

3.8.4 Electronic thermal conductivity. Thermal conductivity is a fundamental parameter of materials. Essentially, there are two main sources of thermal conductivity in materials: (i) electronic charge, which constitutes electronic thermal conductivity, and (ii) lattice vibrations due to the vigorous motion of atoms at their equilibrium sites. Metals are characterized based on the abundance of free electrons. These free electrons are responsible for the conduction of both electrical and thermal energies. Meanwhile, in semi-metals and semiconductors, heat transfer is carried by both electrons as well as holes. The variation of the electronic thermal conductivity of the alloys under study is plotted and is shown in Fig. 13a–c. For the semiconducting channel, it is evident that increasing temperature raises κ_e with a minimum occurring near zero chemical potential. The increasing nature is attributed to the excited electrons and holes. It is also evident from the Fig. 13 that σ and κ_e exhibit similar trends.

Fig. 14 gives an estimation of the lattice thermal conductivity through Slack's equation. The lattice part of the thermal conductivity is determined by Slack's equation:[37]

$$k_l = \frac{A\theta_D{}^3 V^{\frac{1}{3}} m}{\gamma^2 N^{\frac{2}{3}} T}$$

The parameters used in this equation are the Grüneisen parameter (γ), the number of atoms per unit cell (N), the Debye temperature (θ_D), volume (V), and the average molar mass per atom (m). The value of A used in this equation is γ-dependent and is defined as; $A = \dfrac{2.43 \times 10^{-8}}{1 - \dfrac{0.514}{\gamma} + \dfrac{0.228}{\gamma^2}}$. The obtained κ_l from this equation is shown in Fig. 14. It can be observed from the plots that κ_l demonstrates a decreasing trend. These values of lattice thermal conductivity are used to evaluate the dimensionless figure of merit at the mentioned temperature.[38–40]

3.8.5 Thermoelectric figure of merit (ZT). The graphical variation of the thermoelectric figure of merit with chemical potential is depicted in Fig. 15a–c. It is evident from the plots that ZT is the lowest at 300 K. This is mainly attributed to high lattice thermal conductivity. The ZT increases readily with temperature at 600 K, which is due to the decrease in kappa, and it does not show a significant rise at 900 K, which can be attributed to the abrupt increase in electronic thermal conductivity. As the thermoelectric parameters S, σ and k alter differently with temperature, it is challenging to find the ZT, which is constant over a significant range.

4. Conclusion

The present study is performed by employing two different powerful DFT methods, GGA and mBJ, with the aim of understanding the potential applications of alloys in spin-dependent and thermoelectric devices. The results obtained confirm the applications of alloys in spintronics and other spin-dependent devices. The alloys were found to exhibit a non-magnetic semi-metallic nature and crystallize in a non-centrosymmetric structure. Furthermore, the alloys follow all mechanical stability and structural criteria and also have a ductile nature, which confirms the applications of alloys under high stresses and strains. They also behave as anisotropic media for different longitudinal and transverse sound velocities, and their calculated magnitudes are presented in Tables 3–5. The bonding nature is mixed, which has been confirmed by Poisson's ratio and electron density contour plots; hence, the alloys are categorized as polar covalent. All the alloys have a high figure of merit (ZT), which guarantees applications in thermoelectric technology.

Conflicts of interest

The authors declare that they have no conflict of interest for this work.

Data availability

The data would be available from the corresponding author on a reasonable request.

Acknowledgements

References

1 D. Abdullah and D. C. Gupta, Exploring the half-metallic ferromagnetism, dynamical and mechanical stability, optoelectronic and thermoelectric properties of K2NaMI6 (M= Mn, Co, Ni) for spintronic applications, *Sci. Rep.*, 2023, **13**(1), 12795.

2 W. Han, Y. C. Otani and S. Maekawa, Quantum materials for spin and charge conversion, *npj Quantum Mater.*, 2018, **3**, 1–16.

3 B. Dieny, *et al.*, Opportunities and challenges for spintronics in the microelectronics industry, *Nat. Electron.*, 2020, **3**, 446–459.

4 M. N. Baibich, *et al.*, Giant magnetoresistance of (001)Fe/(001)Cr magnetic superlattices, *Phys. Rev. Lett.*, 1988, **61**, 2472–2475.

5 G. Binasch, P. Grünberg, F. Saurenbach and W. Zinn, Enhanced magnetoresistance in layered magnetic structures with antiferromagnetic interlayer exchange, *Phys. Rev. B:Condens. Matter Mater. Phys.*, 1989, **39**, 4828–4830.

6 L. Chang, M. Wang, L. Liu, S. Luo and P. Xiao, A brief introduction to giant magnetoresistance, *arXiv*, 2014, preprint, arXiv:1412.7691, DOI: 10.48550/arXiv.1412.7691.

7 M. Tsoi, et al., Excitation of a magnetic multilayer by an electric current, Phys. Rev. Lett., 1998, **80**, 4281–4284.

8 J. A. Katine, F. J. Albert, R. A. Buhrman, E. B. Myers and D. C. Ralph, Current-driven magnetization reversal and spin-wave excitations in Co/Cu/Co pillars, Phys. Rev. Lett., 2000, **84**, 3149–3152.

9 G. Schmidt, Concepts for spin injection into semiconductors-a review, J. Phys. D Appl. Phys., 2005, **38**, R107.

10 Z. Wilamowski and A. M. Werpachowska, Spintronics in semiconductors, Mater. Sci. Pol., 2006, **24**, 803–808.

11 H. E. Ferromagnets, D. Miller, I. Le Breton-Miller and R. H. Lester, correction to "Family Ownership and Acquisition Behavior in Publicly-Traded Companies" (D. Miller, I. Le Breton-Miller and R. H. Lester), Strateg. Manag. J., 2010, **31**, 347.

12 D. Awschalom and N. Samarth, Spintronics without magnetism, Physics, 2009, **2**, 50.

13 Y. K. Kato, R. C. Myers, A. C. Gossard and D. D. Awschalom, Observation of the spin hall effect in semiconductors, Science, 2004, **306**, 1910–1913.

14 J. Fabian, A. Matos-Abiague, C. Ertler, P. Stano and I. Žutić, Semiconductor spintronics, Acta Phys. Slovaca, 2007, **57**, 565–907.

15 W. H. Butler, X. G. Zhang, T. C. Schulthess and J. M. MacLaren, Spin-dependent tunneling conductance of Fe/MgO/Fe sandwiches, Phys. Rev. B:Condens. Matter Mater. Phys., 2001, **63**, 544161–5441612.

16 L. Gitelman, Paper Knowledge: Toward a Media History of Documents, Duke University Press, 2014.

17 S. Chen, et al., Effect of Hf concentration on thermoelectric properties of nanostructured n-type half-heusler materials HfxZr1-xNiSn 0.99Sb0.01, Adv. Energy Mater., 2013, **3**, 1210–1214.

18 J. P. Perdew, K. Burke and M. Ernzerhof, Generalized gradient approximation made simple, Phys. Rev. Lett., 1996, **77**, 3865–3868.

19 A. D. Becke and E. R. Johnson, A simple effective potential for exchange, J. Chem. Phys., 2006, **124**(22), DOI: 10.1063/1.2213970.

20 F. Tran, P. Blaha and K. Schwarz, Band Gap Calculations with Becke–Johnson Exchange Potential, 2007, p. 196208.

21 D. Koller, F. Tran and P. Blaha, Improving the modified Becke-Johnson exchange potential, Phys. Rev. B: Condens. Matter Mater. Phys., 2012, **85**(15), 155109.

22 M. El Goutni, M. Batouche, H. Ferjani, T. Seddik and D. Abdullah, Advancing sustainable energy: Photocatalytic and thermoelectric properties of Cs₂MBr₆ double perovskites (M= Re4+, W4+, Ru4+, Os4+), Inorg. Chem. Commun., 2025, 115644.

23 G. K. H. Madsen, J. Carrete and M. J. Verstraete, BoltzTraP2, a program for interpolating band structures and calculating semi-classical transport coefficients, Comput. Phys. Commun., 2018, **231**, 140–145.

24 T. Graf, C. Felser and S. S. P. Parkin, Simple rules for the understanding of Heusler compounds, Prog. Solid State Chem., 2011, **39**, 1–50.

25 F. Mouhat and F. X. Coudert, Necessary and sufficient elastic stability conditions in various crystal systems, Phys. Rev. B:Condens. Matter Mater. Phys., 2014, **90**(22), 224104.

26 D. Abdullah and D. C. Gupta, Structural, mechanical and dynamical stabilities of K_2NaMCl_6 (M: Cr, Fe) halide perovskites along with electronic and thermal properties, J. Magn. Magn. Mater., 2023, **569**, 170474.

27 D. Abdullah and D. C. Gupta, Probing the structural, opto-electronic, mechanical, and thermoelectric properties of novel lead-free semiconductor double perovskites Rb_2MgMnX_6 (X= Cl, Br, I): first principle study, J. Mater. Res., 2024, **39**(2), 262–272.

28 A. Quyoom Seh and D. C. Gupta, Comprehensive DFT investigation of transition-metal-based new quaternary Heusler alloys CoNbMnZ (Z= Ge, Sn): Compatible for spin-dependent and thermoelectric applications, RSC Adv., 2020, **10**(71), 43870–43881.

29 Download_Center@chem.libretexts.org.

30 W. H. Eugen Schwarz, The full story of the electron configurations of the transition elements, J. Chem. Educ., 2010, **87**, 444–448.

31 trends_electronegativity @ https://www.angelo.edu.

32 B. S. Park, The contexts of simultaneous discovery: Slater, Pauling, and the origins of hybridisation, Stud. Hist. Philos. Sci. B., 2000, **31**(4), 451–474.

33 Charge-density analysis of bonding in Laves phases, Google Search, https://www.google.com/search?q=(Charge-density+analysis+of+bonding+in+Laves+phases).&oq=(Charge-density+analysis+of+bonding+in+Laves+phases).&aqs=chrome..69i57.1677j0j15&sourceid=chrome&ie=UTF-8.

34 S. B. Riffat and X. Ma, Thermoelectrics: a review of present and potential applications, Appl. Therm. Eng., 2003, **23**, 913–935.

35 X. Zhang and L. D. Zhao, Thermoelectric materials: Energy conversion between heat and electricity, J. Mater., 2015, **1**, 92–105.

36 S. A. Mir and D. C. Gupta, Analysis of Cage Structured Halide Double Perovskites Cs2NaMCl6 (M = Ti, V) by Spin Polarized Calculations, J. Alloys Compd., 2021, **854**, 156000.

37 G. A. Slack, The Thermal Conductivity of Nonmetallic Crystals, Solid State Phys.–Adv. Res. Appl., 1979, **34**, 1–71.

38 H. Van Ngoc. and H. T. P. Thuy, Investigation of Be, Mg, Ti–adsorbed boron-germanene nanoribbons for nano applications, J. Phys.: Condens. Matter, 2024, **36**(50), 505901.

39 H. Van Ngoc. and H. T. P. Thuy, Group I elements-adsorbed NiZnO monolayer: Electro-optical properties and potential applications, Phys. B, 2025, **700**, 416922.

40 H. Van Ngoc. and H. T. P. Thuy, Study of NO, CO, and CO2 gas adsorption on Ni-doped ZnO monolayers for sensing applications, Chem. Phys. Lett., 2025, **868**, 142020.